RESEARCH ARTICLE

ADVANCED OPTICAL MATERIALS
www.advopticalmat.de

A Simplified Model for Polycrystalline $BaTiO_3$ Nanoresonator for Second Harmonic Generation

Andrea Tognazzi, Paolo Franceschini, Helena Weigand, Ülle-Linda Talts, Alfonso Carmelo Cino, Rachel Grange, and Costantino De Angelis*

Second Harmonic Generation (SHG) has become a critical technique in material characterization, image processing and microscopy. While bulk crystals have been traditionally used for SHG due to their high conversion efficiencies, limited control over radiation properties, delicate phase-matching conditions and alignment pose significant challenges. The exploration of nanoscale materials and structures based on dielectric platforms has provided enhanced SHG efficiency and control, but their limited transparency in the visible spectral range and complex fabrication processes hinder broader application. Barium titanate ($BaTiO_3$), a ferroelectric material with spontaneous polarization and nonlinear optical behavior, presents an attractive alternative due to its suitability for nano-imprinting techniques, facilitating scalable production of metasurfaces. In this study, SHG from single polycrystalline $BaTiO_3$ nanocylinders is investigated. Through polarization-dependent experiments, the influence of crystalline domain orientation and arrangements within the nanocylinders on SHG efficiency is characterized. A simplified numerical model to interpret the different polarization-dependent SHG diagrams obtained from nominally identical nanocylinders is developed. The results reveal the significant impact of domain geometry and relative size on SHG characteristics. By understanding the relationship between domain geometry and SHG giving insights into the material characterization and design optimization of $BaTiO_3$ and other polycrystalline nanostructures in nonlinear optical devices.

1. Introduction

Second Harmonic Generation (SHG) has emerged as a powerful tool in various fields, including material characterization,[1] image processing,[2] microscopy[3] and information storage.[4] The traditional bulk crystals, which can achieve large conversion efficiencies due to phase matching, offer limited control over the radiation properties of the generated light. The exploration of nanoscale materials and structures has opened new avenues for enhancing SHG efficiency and control, extending the landscape of appealing materials by removing the constraints of phase matching conditions.[5,6] Typically, crystalline dielectrics with high refractive index such as gallium arsenide (GaAs) and aluminium gallium arsenide (AlGaAs) are used in metasurfaces and single nanostructures to achieve tailored SHG responses by strongly confining the electromagnetic (EM) field inside the material.[7–14] However, their transparency region is limited and hinders efficient SHG in the visible spectrum.[15] An additional constraint of such platforms is related to the poor scalability and difficult nanofabrication processes, relying on mono-crystalline semiconductor wafers production and electron beam lithography.

Barium titanate ($BaTiO_3$), a well-known ferroelectric material,[16] exhibits spontaneous polarization and nonlinear optical behavior, making it an ideal candidate for SHG applications.[17–19] In addition to its utility in SHG, $BaTiO_3$ can also be utilized to construct modulators,[20–24] further expanding its versatility in photonics due to its ease of tunability. While bulk $BaTiO_3$ exhibits favorably strong second-order coefficients, such as one of the highest known electro-optic coefficients, its fabrication in thin-film form as used for nanophotonics is not yet standardized. While molecular beam epitaxy or physical layer deposition are advantageous for preserving the bulk crystal

A. Tognazzi, A. C. Cino
Universitá degli studi di Palermo
Viale delle Scienze
Palermo 90128, Italy

The ORCID identification number(s) for the author(s) of this article can be found under https://doi.org/10.1002/adom.202402484

DOI: 10.1002/adom.202402484

A. Tognazzi, P. Franceschini, C. De Angelis
Istituto Nazionale di Ottica - Consiglio Nazionale delle Ricerche (INO-CNR)
Via Branze 45, Brescia 25123, Italy
E-mail: paolo.franceschini@unibs.it

P. Franceschini, C. De Angelis
Universitá degli studi di Brescia
Via Branze 38, Brescia 25123, Italy

H. Weigand, Ü.-L. Talts, R. Grange
ETH Zurich, Department of Physics
Institute for Quantum Electronics
Optical Nanomaterial Group
Zurich CH-8093, Switzerland

properties, they are heavy in technical, financial and knowledge-related resources.[25,26] Their use for free-space nanophotonic applications is furthermore limited by the low thin-film thickness and limited substrate compatibility.[27] A more scalable and cost-efficient approach is the use of solution-based $BaTiO_3$, which can be spin-coated in various thicknesses. Solution-based $BaTiO_3$ is available for example via a sol-gel process, which allows next to the previously mentioned benefits a more flexible nanostructuring of this material by exploiting nanoimprint technologies. In contrast to top-down etching technologies, this bottom-up approach enables the fabrication of high-aspect ratio nanostructures, which is limited in e.g. lithium niobate ($LiNbO_3$) metasurfaces so far by sidewall angles resulting from the crystalline materials inertness.[28–32] The use of solution-based $BaTiO_3$ requires an annealing step after the nanostructuring process, to obtain a crystalline, non-centrosymmetric material. The nature of the solution-based approach implies, that the final structures will be polycrystalline, with multiple crystalline domains in different orientations. Probing large volumes of the material, such as in thin-films, allows assuming an effective nonlinear behavior by averaging over the randomly oriented domain tensors. However, such an approximation is not reliable anymore when probing nanostructures on a similar scale as the domain sizes, as the influence of a few domains will dominate the optical response. So far, no model has been presented to cover this intermediate area between average optical properties and monocrystalline behavior. However, in order to efficiently design nonlinear nanophotonic devices, an understanding of the influence of multiple crystal domain orientations is crucial.

Here, we investigate the SHG from single $BaTiO_3$ nanocylinders with radius ranging from 240 to 400 nm. Exploiting polarization-dependent experiments, we address the presence of crystalline domain orientation and arrangements within the single nanocylinders and their influence on SHG efficiency, unveiling the polycrystalline nature of the cylinders. The presence of EM field components along z-axis and multiple domains inside the nanocylinder add additional degrees of freedom, thus further complicating the modeling, design and interpretation of experimental data. Indeed, usually, the modeling of nanoresonators and metasurfaces for nonlinear applications is performed by assuming single-crystal dielectric materials. We develop a simplified numerical model to discuss the origin of the different polarization-dependent SHG response diagrams obtained from nanocylinders of nominally the same size. Previous studies have shown that $BaTiO_3$ nanostructures often possess various domains with distinct orientations.[19] However, the specific impact of these domains on SHG has not been fully explored due to the complexity of a full description taking into account the orientation, position and size of each crystal domain.

Furthermore, we delve into the role of crystal domain geometry and relative size in shaping the SHG characteristics of $BaTiO_3$ nanocylinders. Although the correlation between the SHG anisotropy patterns and the polarization orientation of $BaTiO_3$ was previously studied in ref. [33], nanoresonators offer a richer playground introducing an out-of-plane EM field component that contributes to SHG.

Our study sheds light on the intricate relationship between domain geometry and SHG in $BaTiO_3$ nanocylinders, offering valuable insights for material characterization and the design optimization of nanoscale nonlinear optical materials and devices.

2. Design and Fabrication

2.1. Design

We design resonating nanocylinders for efficient SHG in the visible (VIS) spectral range. First, we investigate the linear optical response of $BaTiO_3$ nanocylinders in the VIS–NIR (near infrared) region via finite element method simulations performed in Comsol Multiphysics. In the presence of a substrate, low refractive index materials necessitate higher height compared to high-refractive index materials to achieve good EM field confinement inside the cylinder. Despite higher cylinders might help to improve EM confinement and exploit higher order multipolar resonances, the fabrication procedure imposes strict limits on the maximum aspect ratios that can be fabricated with high reproducibility. Therefore, we simulate isolated $BaTiO_3$ cylinders placed on a quartz substrate with a height 520 nm (see Supporting Information for more information about height dependence). In **Figure 1a**, we report the normalized scattering cross section as a function of the wavelength for cylinder diameters ranging from 220 to 430 nm. Simulations predict a resonant behavior at $\lambda = 840$ nm for a cylinder diameter $d = 370$ nm. To gain further insights into the EM field distribution at the fundamental frequency, we perform a multipolar decomposition.[34] The results of the analysis at $d = 370$ nm (see Figure 1b) suggest that the resonance at $\lambda = 840$ nm can be ascribed mainly to an electric dipole mode with additional contribution from magnetic dipole and electric quadrupole modes. Moreover, as shown in Figure 1c and d, the field enhancement distribution confirms the contribution from the aforementioned multipolar modes within the nanocylinders.

2.2. Fabrication

The nanocylinders were fabricated using a bottom-up fabrication approach with solution-based $BaTiO_3$. To this end, a sol-gel synthesis was performed in analogy to the process described in ref. [35]. The solution was filtered by a 0.4 µm PTFE-membrane and subsequently spin-coated on a double-side polished quartz substrate of 1 mm thickness. The nanocylinders were fabricated by nanoimprinting the solution with a pre-structured, flexible plastic stamp. This stamp was previously molded from a nanostructured master, which was fabricated with electron-beam lithography. Details of the master and stamp fabrication can be found in Ref. [36]. After hardening of the imprinted $BaTiO_3$ solution, the plastic stamp was removed and the $BaTiO_3$ nanocylinders were annealed at 700°C to form a non-centrosymmetric, polycrystalline material.[36] The resulting $BaTiO_3$ structures have a refractive index of 1.9 at $\lambda = 900$ nm, which is higher than previously reported $BaTiO_3$ nanoparticle films due to an increased material density.[24,37] This increased density is enabled by a shrinking process during the annealing, which decreases the structure size by 40% as compared to the initial design. This is compensated in the initial master mold by correspondingly increased

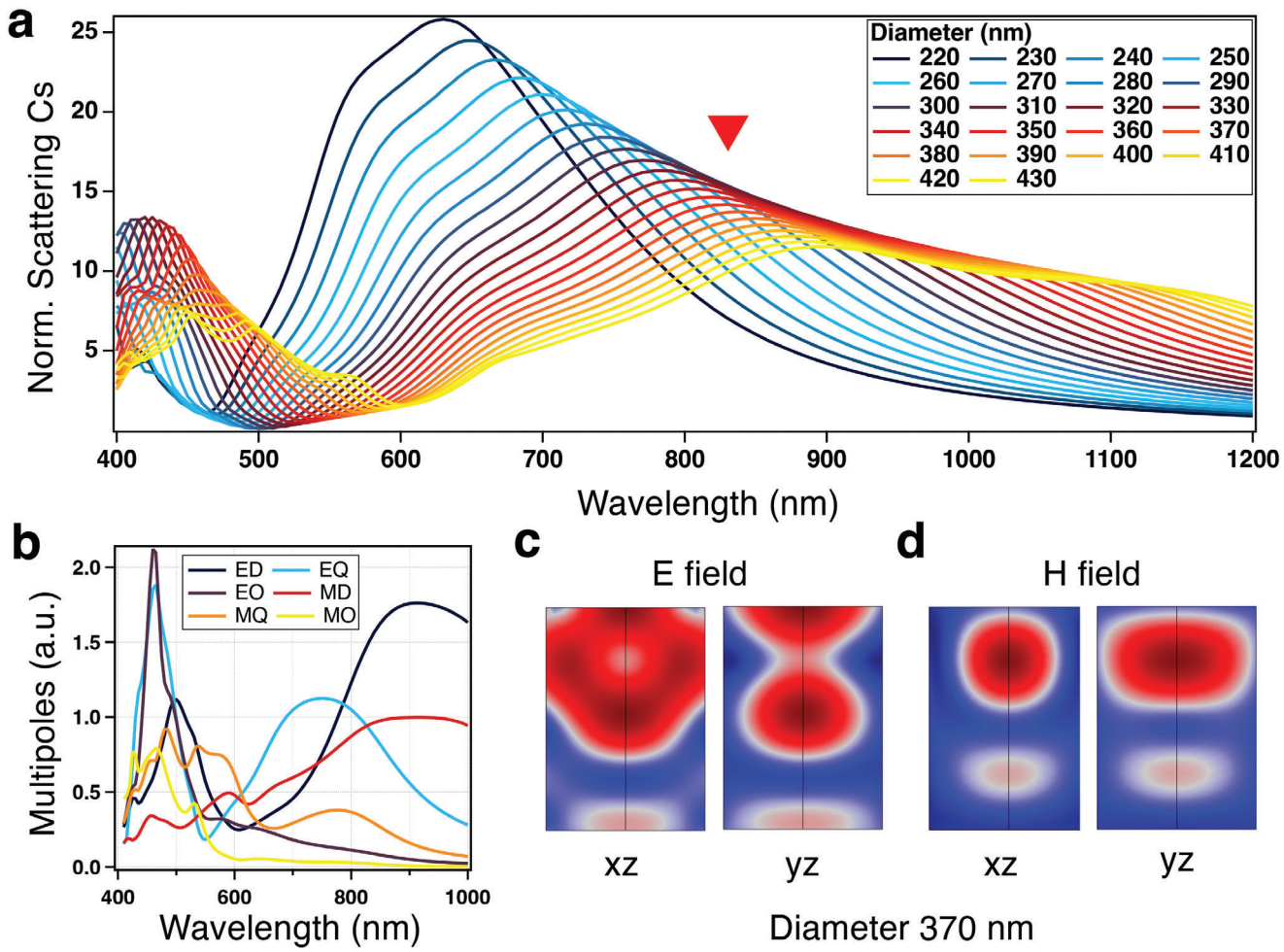

Figure 1. a) Normalized scattering cross section as a function of the wavelength for diameter values ranging from 220 to 430 nm of a cylinder with height 520 nm. The red triangle indicate the pump frequency of 840 nm employed in the second harmonic generation experiments. b) Multipolar decomposition of the electromagnetic field of the cylinder with 370 nm diameter. c) Corresponding electric field distribution at 840 nm along the *xz* and *yz* plane, respectively. d) Magnetic field distribution along the *xz* and *yz* plane, respectively.

dimensions to realize the designed cylinder sizes. The fabricated sample features cylinders with different height and diameter (175–400 nm), while each cylinder diameter was reproduced 16 times to allow multiple optical measurements (the sixteen replicas are arranged in a checkerboard pattern, with nearest-neighbors being 10 µm apart). In contrast to top-down etching of inert metal-oxides, which is often limited by the sidewall angles intrinsic to physical etching,[38] the aspect ratios achieved here are above 2. As can be seen from **Figure** 2a, the sidewalls from the nanoimprinted $BaTiO_3$ nanocylinders are completely perpendicular to the substrate and feature a smooth surface. The domains of polycrystalline $BaTiO_3$ inside the cylinders will be arbitrarily oriented with respect to each other. This necessitates the need for a theoretical understanding of the influence of domain orientations on the SHG intensity and polarization dependence, in order to efficiently design nonlinear optical devices from this promising material platform.

3. Second Harmonic Generation in $BaTiO_3$ Nanoresonators

The nonlinear optical properties of single $BaTiO_3$ nanocylinders have been experimentally investigated by a nonlinear microscopy setup working in transmission geometry. A linearly-polarized beam at the fundamental wavelength ($\lambda_p = 840$ nm) impinges at normal incidence on the back side of the sample (substrate side) and then resonantly excites the individual nanocylinder with a spot size (beam waist) of $w_0 = (7.5 \pm 0.5)$ µm (see Experimental Section for additional details). The transmitted nonlinear signal is collected by a high-NA (numerical aperture, 0.85) objective and measured by a single photon avalanche detector. The residual beam at the fundamental frequency is filtered out by a series of shortpass filters (400–500 nm spectral region) before the detector (see Experimental Section for additional details). To clarify the nature of the radiated light, we perform power-dependent measurements on a single nanocylinder with illumination power

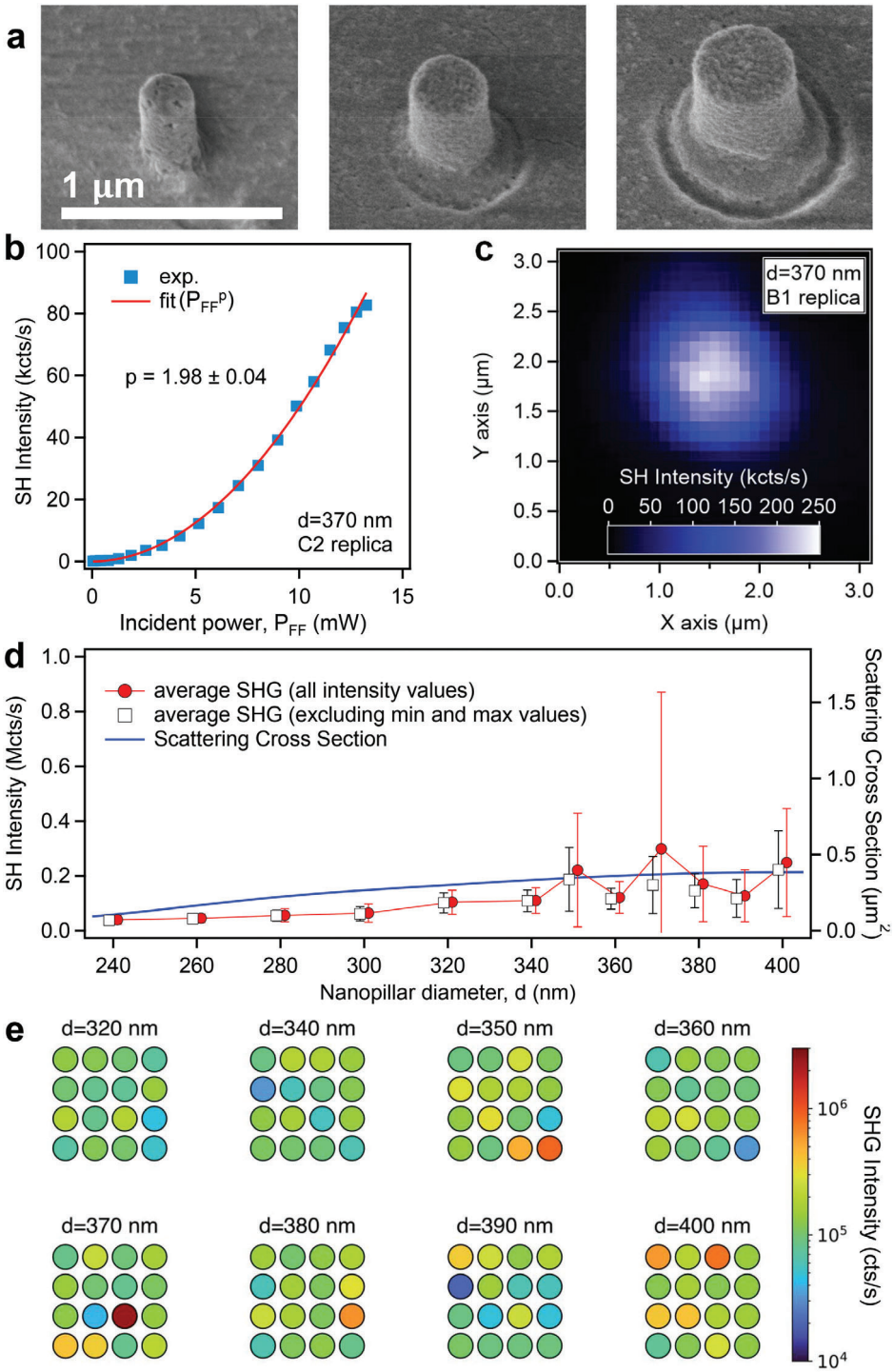

Figure 2. a) Scanning electron micrograph of the fabricated $BaTiO_3$ cylinders with different size. b) Second harmonic (SH) intensity as a function of the average incident pump power (blue markers) and quadratic power fit (red). c) Spatially-resolved scan of the SH radiation intensity emitted by a cylinder with diameter 370 nm for an illumination power P_{FF} = 13.3 mW. The substrate SH is three order of magnitude smaller than the SH generated in the presence of the nanocylinder. d) Size-dependent mean SH intensity value (left axis) obtained as the average over two sets of cylinder replicas (experimental measurement P_{FF} = 13 mW): whole set of sixteen replicas within the pad (red markers) and subset of fourteen replicas (black markers), where the latter dataset has been obtained by removing the minimum and maximum SH intensity values from the former one. The error bars represent the standard deviation calculated over the considered replicas. Calculated scattering cross section as a function of the cylinder diameter (blue solid line, right axis). e) Overview of the SH intensity signal (colorscale) measured from cylinders with the same size (sixteen replicas for each diameter value). Each colored circle represents one cylinder. Each set of sixteen pillars (forming a square) represents a pad with the diameter value indicated in the label (P_{FF} = 13 mW).

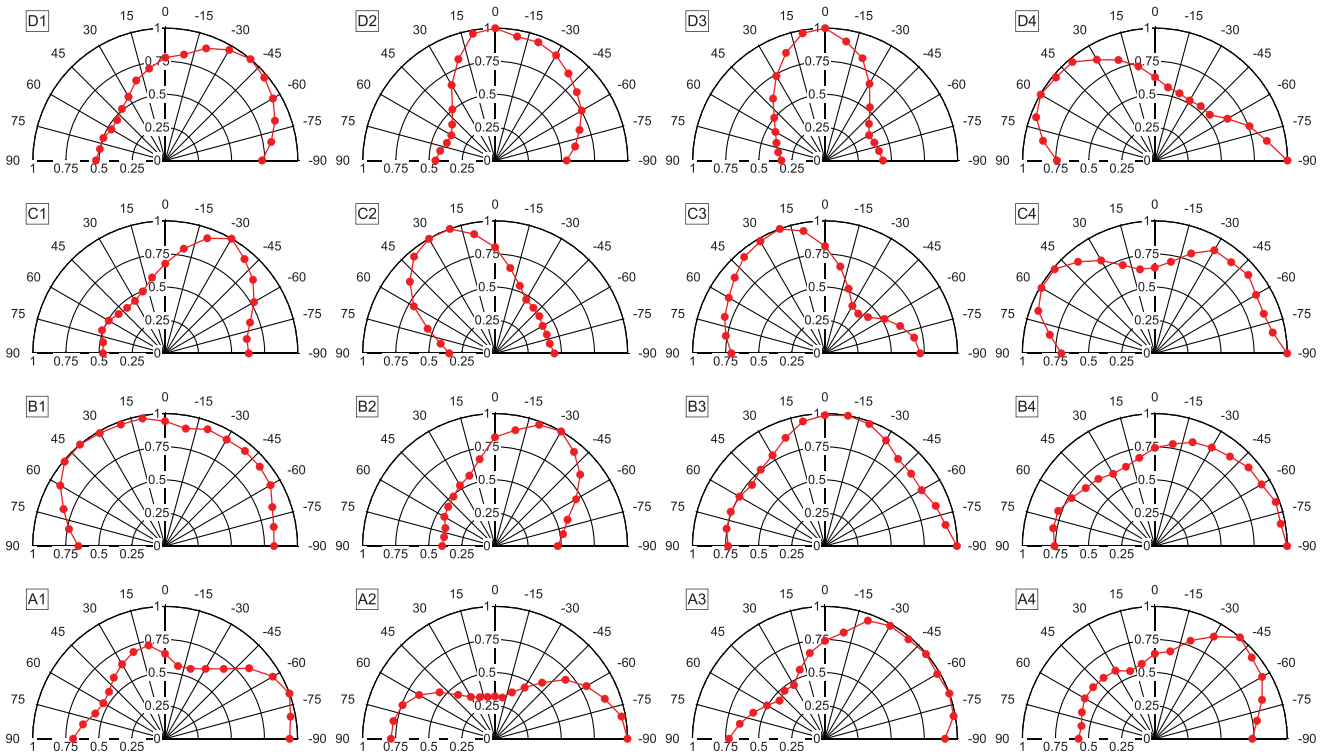

Figure 3. Normalized second harmonic as a function of the pump polarization angle (φ). The polar plot are obtained by replicas of nominally identical cylinders with diameter 400 nm.

(P_{FF}) ranging from 0.04 to 13.3 mW, whose results are reported in Figure 2b (markers). The quadratic fit (red solid line) to the experimental data confirms the second-order origin of the process, thus SHG. Moreover, space-resolved SHG measurements on individual nanocylinder (see Figure 2c) shows that the SH from the surrounding BaTiO3 thin-film is three orders of magnitude lower (comparable to the detector thermal noise). Here we note that, in Figure 2c, the SHG signal spatially extends to an area which is larger than the nanoresonantor one, which is due to the smaller size of cylinder compared to the beam spot size. The finite-size of the cylindrical geometry gives rise to an EM field component along the *z*-axis within the nanocylinder, which in turn induces nonlinear currents that are responsible for the SHG process.[8] Moreover, the extremely low-intensity signal from the thin-film also suggests that the SHG process can be fully ascribed to a volumetric contribution (rather than surface one). To study the enhancement of the SHG signal due to the presence of multipolar modes, we measure SHG from nanocylinders with diameters ranging from 240 to 400 nm. Figure 2d displays the dependence of the experimentally detected SHG (mean value over sixteen replicas) as a function of the diameter size upon illumination at $\lambda_p = 840$ nm wavelength with linearly-polarized light at a fixed angle.

The comparison between the experimental data (mean value) and the calculated scattering cross-section profile (blue line in Figure 2d) shows good agreement, i.e., the SHG signal increases in correspondence with the resonant cylinder diameter; however, we observe a large dispersion of the SHG signal detected from the various replicas, as shown by the error bars in Figure 2d, which can be better visualized in Figure 2e. We underline that the various replicas may have small differences in the geometry due to the fabrication process and these could lead to variations of the detected second harmonic (SH) in nominally identical cylinders (under the same excitation conditions). However, the amplitude of such differences is much smaller than the one measured here. Taking into account the structural properties of the system under analysis, the observed behavior may be ascribed to a different orientation of the crystalline domains in the various replicas. Such a hypothesis is supported by previous studies on thin-film structures deposited with similar annealing conditions, where the authors have shown that the expected grain sizes are ≈35–70 nm, resulting in these nanocylinders potentially having contributions from up to hundreds of domains.[39] Therefore, to investigate the effect of crystalline domain orientation on SHG from single $BaTiO_3$ nanocylinders, we performed polarization-resolved SH measurements by collecting the nonlinear signal at various pump polarization angles (φ).

The pump-polarization-dependent SH intensity obtained for the sixteen replicas of the 400-nm-size cylinder are displayed in **Figure 3** as polar plots. Clearly the variety of measured profiles suggests that the replicas return different responses upon the same excitation conditions. Therefore, the different replicas have a different composition in terms of crystalline domain orientation. At this stage, it is worth mentioning that within a single cylinder, more than one crystalline domain could be present.

To further elucidate the origin of the SH intensity value dispersion in Figure 2, we perform numerical simulations of the SHG process, in which we calculate pump-polarization

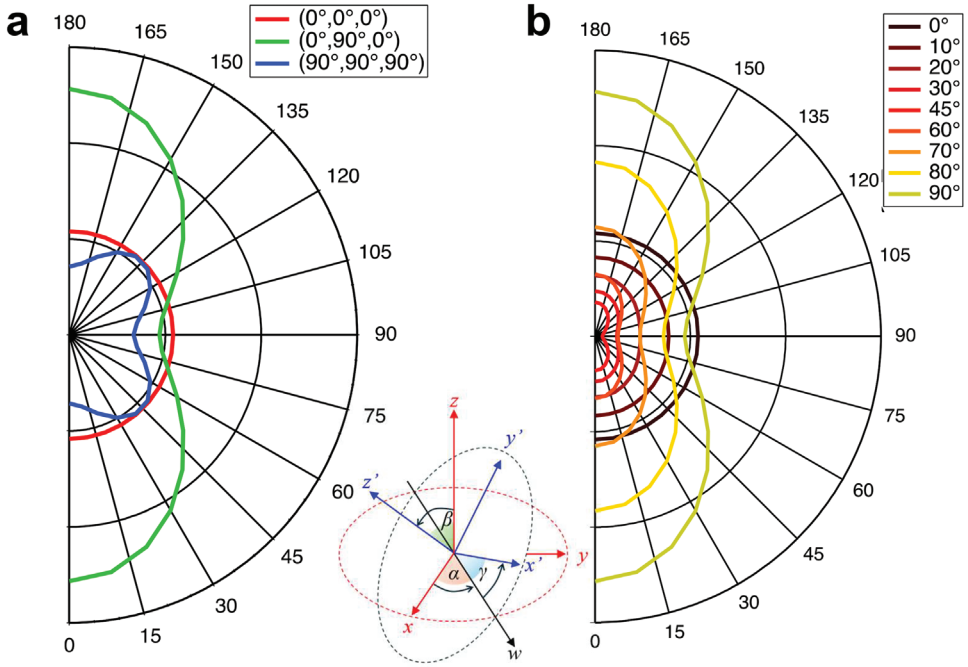

Figure 4. Calculated second harmonic intensity diagrams for monoscrystalline $BaTiO_3$ nanocylinder. a) The crystalline domain orientations are (α, β, γ) = (0°, 0°, 0°), (α, β, γ) = (0°, 90°, 0°), and (α, β, γ) = (90°, 90°, 90°), which are depicted in red, green and blue, respectively. b) The crystalline domain orientations is (0°, β, 0°), with β ranging from 0° to 90°.

dependent SHG intensity diagrams for $BaTiO_3$ nanocylinders with different domain composition (see Experimental Section section for more details). The spatial orientation of the crystalline domain within a cylinder is described through Euler's angles α, β, and γ, as sketched in the inset of **Figure** 4a.

First, we focus on the case in which the whole cylinder is monocrystalline. Figure 4a displays the calculated pump-polarization dependent SH intensity diagrams for three domain orientations: (α, β, γ) = (0°, 0°, 0°), (0°, 90°, 0°), and (90°, 90°, 90°). Clearly, the reported diagrams exhibit strong differences regarding both angular dependence and signal amplitude. Indeed, while the (0°, 0°, 0°) profile is isotropic, on the other hand (0°, 90°, 0°) and (90°, 90°, 90°) profiles show significant angular dependence. For completeness, it is useful to note that the configuration (0°, 0°, 0°), describing the case in which the propagation direction of the impinging EM field is parallel to the domain orientation, gives rise to a SH intensity diagram analogous to the one obtained for bulk $BaTiO_3$[16] with the same geometry. Moreover, Figure 4b details the evolution of the SH intensity profiles for the (0, β, 0) configuration, with β ranging from 0° to 90°. We observe that the minimum SH amplitude is achieved for $\beta \sim 45°$. Therefore, the numerical results in Figure 4 allow concluding that the large variation in the SH intensity reported in Figure 2 for cylinders with the same size can be ascribed to the presence of different crystalline domain orientations among the various replicas. Although the calculated profiles in Figure 4 are similar to some of the measured ones (Figure 3), the former are not detailed enough to provide a comprehensive explanation, since they do not fully reproduce the asymmetric behavior (with respect to $\varphi = 0°$) occurring in some of the experimental diagrams.

Therefore, we perform numerical simulations in which the nanocylinder features two domains with different crystal orientations. First, we consider domains with the same volume. As shown in the inset of **Figure** 5a, the two subregions within the nanocylinder are obtained by partitioning the cylinder with a plane, the latter passing through the center of the former, at an angle θ with respect to the z-axis. At first, we consider domains defined by (α_A, β_A, γ_A) = (0°, 0°, 0°) and (α_B, β_B, γ_B) = (90°, 90°, 90°), where the subscripts letter refers to the domain. Thus for $\theta = 0°$ ($\theta = 90°$) the cylinders are partitioned by a vertical (horizontal) plane. The red, black and blue lines in Figure 5a correspond to $\theta = -40°$, 0°, 40°, respectively. The presence of a second crystalline domain of equal size introduces an asymmetry in the diagram that depends on the spatial distribution of the domains. Such asymmetric behavior is also present in the experimental SHG profiles and thus suggests a multi-domain composition of the fabricated nanocylinders. We note that for $\theta = 40°$ and $\theta = -40°$ the SH polarization dependence is different. This is because, as can be seen in Figure 1, the electric field is mainly localized in the upper portion of the pillar. Therefore, positive and negative values of θ weights differently the contributions from domains A and B. This suggests that the domains localized in the hotspots of the EM fields have a greater influence on the value and polarization dependence of SHG. To further prove this point, we investigated the configuration in which the two domains occupy regions with different volumes by keeping the same domain shape. For simplicity, this can be achieved by shifting the partition plane along the y-axis at fixed θ angle (see sketch in Figure 5b). The change in the relative size of the domains results in a variation in the maximum efficiency. However, for shifts of ±50 nm, the polarization

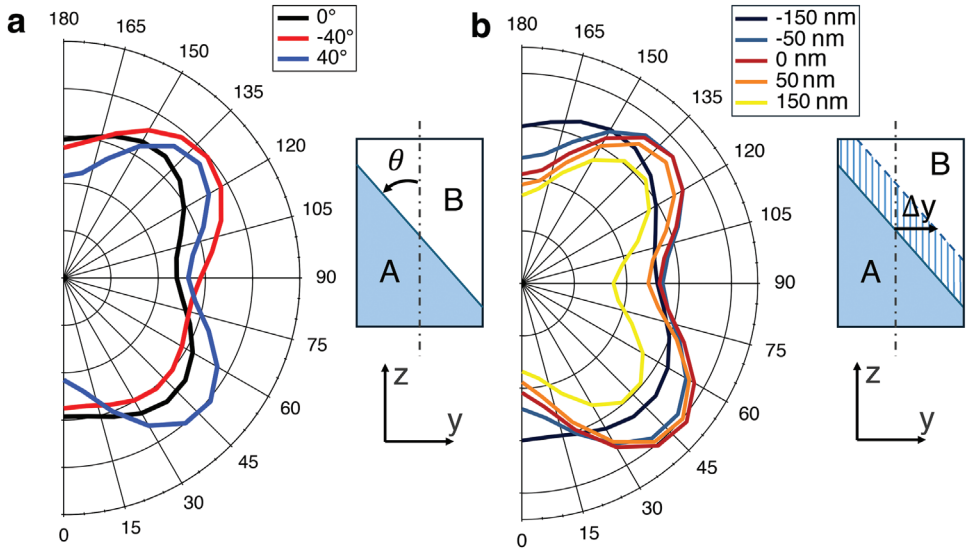

Figure 5. Calculated SH intensity diagrams for $BaTiO_3$ nanocylinder with two-domains of equal volumes. The black line corresponds to a vertically partitioned cylinder ($\theta = 0°$). The blue and red lines correspond to a partitioning plane with angles +40° and –40°, respectively. b) Calculated SH intensity diagrams for $BaTiO_3$ nanocylinder with two-domains of different volumes. A plane partitioning the cylinder at $\theta = +40°$ is shifted along the *y*-axis, which corresponds to a change in the relative volumes between domains A and B.

dependence of SH is nearly unaffected. This is due to the fact that the hotspot close to the top of the cylinder along the axis remain in the same domain (B). Additional results regarding the influence of shape and domain position can be found in the Supporting Information.

Although the two-domain-based model unveils that the asymmetry in the pump-polarization dependent SH intensity profiles is due to a multi-domain nature of the cylinders, the asymmetry resulting from the numerical simulations is much lower than the measured one. Therefore, we consider a design in which the cylinder volume is divided into four regions, as shown in the bottom of **Figure 6**, generated by two planes passing through the center and the edges of the cylinder. Figure 6a displays the polarization diagrams obtained for exemplary configurations of domain orientations (0°, 0°, 0°) and (90°, 90°, 90°) within the cylinder, as sketched in the bottom line. As expected, when the domains are symmetric with respect to the vertical axis, as A1 and A3, the SH diagram is symmetric. Configurations A2 and A4 correspond to the same domain distribution but with opposite domain composition. Both of them have an asymmetric SH diagram but A2 presents a significantly larger asymmetry. This is due to the uneven distribution of the electric field along the *z*-axis (see Figure 1), which results in a different contribution from the domain in the lower and upper part of the cylinder. The numerical results suggest that the presence of multiple crystalline domains within the structure have varying contributions to the SH profiles. Here, we show how the unique asymmetric polarization dependence can be modeled by a simplified structure made of four domains with equivalent volume but varying crystalline orientation. In Figure 6b, we report the polarization diagrams for a configuration involving two different domain orientations, this time with contributing domains having an orientation of (0°, 90°, 0°) or (90°, 90°, 90°), indicated in pink and white color respectively. Here, the efficiency along the same direction changes by a factor of 2 even if the angular dependence of the polarization is similar, highlighting that the domain orientation not only affects the angular polarization dependence but the efficiency itself. Moreover, the comparison of configuration B3 and B4 show that the domain position is a key factor that strongly affect the SH efficiency due to the non-homogeneous distribution of the electric field inside the nanoresonator.

4. Conclusion

In our work, we demonstrated how to exploit polycrystalline $BaTiO_3$ nanocylinders to enhance SHG in the visible region. A simple, yet effective model, revealed the key role of crystalline domain orientations in shaping the SHG pump polarization dependence. We identified that the largest contribution to SHG is largely determined by the crystalline phases in the hotspots at the fundamental frequency field. Additionally, we revealed that the local crystal orientation is a key factor to control polarization dependence and SH efficiency of nanostructures. Our work has potential applications beyond nonlinear frequency generation by providing a simple method to distinguish single crystal structures by means of nondestructive measurements with visible light and providing a measurements-backed simplified modeling approach for polycrystalline nanostructures.

5. Experimental Section

Second Harmonic Generation: A home made microscope was employed to perform SHG measurement. The output of an OPA (Opera-F, Coherent), with a repetition rate 500 kHz, was filtered by a band pass filter at 840 nm (Thorlabs, FBH840-10) and the intensity was controlled by an half-waveplate (Thorlabs, AHWP05M-980) and a polarizer

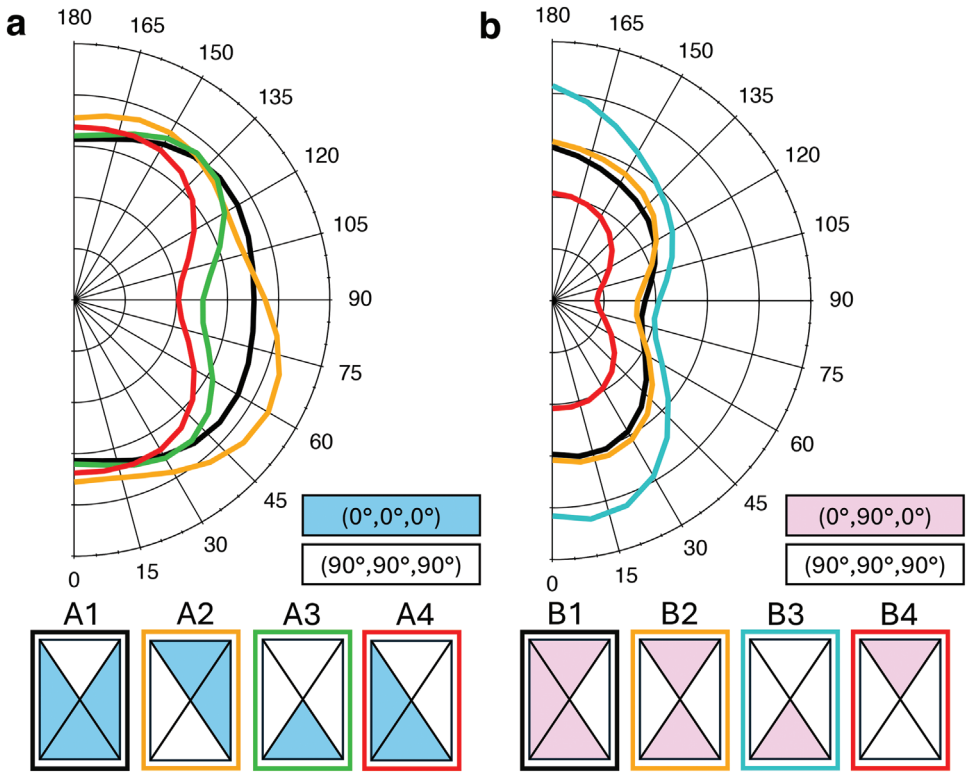

Figure 6. a) Calculated second harmonic as a function of pump polarization angle. The sketches represent the crystal orientation of each domain, where blue and white correspond to (0°, 0°, 0°) or (90°, 90°, 90°), respectively. b) Calculated second harmonic as a function of pump polarization angle. The sketches represent the crystal orientation of each domain, where pink and white correspond to (0°, 90°, 0°) or (90°, 90°, 90°), respectively.

(Thorlabs, GL10). The pump polarization was rotated by an additional half-waveplate to avoid beam displacement. Spatial filtering was performed to improve the beam profile quality by means of a two lens telescope (Thorlabs, LA1131) and a 50 µm diameter pinhole (Thorlabs, P50D). The light was focused on the sample by a 35-mm-focal-length lens (Thorlabs, LA1027) and the resulting spot size was $w_0 = (7.5 \pm 0.5)$ µm, with w_0 being the beam waist of the intensity profile at focus. The emitted SH was collected by a large numerical aperture objective (Olympus, LCPLN100XIR, 100x NA = 0.85) and routed toward a single photon avalanche detector (MPD, PD-50-0TD). The fundamental wavelength was filtered by a set of short pass filters (Thorlabs, FESH0450, FESH0500, FESH0550, FGB18S). The value of the emitted SH signal from each nanocylinder was measured 10 times. Each single measurement was obtained with 1 sec exposure time. In order to calculate the emitted SH intensity value, the measured SH intensity value was refined taking into account the optical losses ($c_{loss} = 0.036$) due to the detection system. See Supporting Information for the sketch of the experimental setup.

Numerical Simulations: Numerical simulations were performed using Comsol Multiphysics. A maximum mesh size five times smaller than the SH wavelength and a domain size larger than 2.1 times the fundamental wavelength were employed. The refractive index of the substrate was set to 1.537. A planewave impinging normally to the surface illuminates the cylinder from the substrate side at frequency ω. The electric field at the fundamental frequency was employed to calculate the nonlinear currents considering the vectorial nature of the SH response. Inside the resonator, the EM field was rotated at the fundamental frequency in a new reference system, by means of Euler's angles, to calculate the induced nonlinear currents for a rotated crystal domain. The calculated nonlinear currents were then rotated back to the original reference system and the electromagnetic problem was solved at the SH frequency 2ω. The multipolar decomposition was performed by projecting the calculated scattered field at the fundamental frequency on the corresponding spherical harmonics as described in ref. [34].

Supporting Information

Supporting Information is available from the Wiley Online Library or from the author.

Acknowledgements

A.T. acknowledges the financial support from the European Union through "FESR o FSE, PON Ricerca e Innovazione 2014-2020 - DM 1062/2021" and the University of Palermo through "Fondo Finalizzato alla Ricerca di Ateneo 2024 (FFR2024)." H.W. acknowledges support from the physics department of ETH Zurich. This work was partially supported by the European Union under the Italian National Recovery and Resilience Plan (NRRP) of NextGenerationEU, of partnership on "Telecommunications of the Future" (PE00000001 - program "RESTART"), S2 SUPER – Programmable Networks, Cascade project PRISM - CUP: C79J24000190004.

Open access publishing facilitated by Universita degli Studi di Brescia, as part of the Wiley - CRUI-CARE agreement.

Conflict of Interest

The authors declare no conflict of interest.

Data Availability Statement

The data that support the findings of this study are available in the supplementary material of this article.

Keywords

$BaTiO_3$, nanophotonics, second harmonic generation

Received: September 13, 2024
Revised: November 20, 2024
Published online: December 25, 2024

[1] F. Simon, S. Clevers, V. Dupray, G. Coquerel, *Adv. Chem. Technol.* **2015**, *38*, 971.
[2] L. Hong, F. Lin, X. Qiu, L. Chen, *Appl. Phys. Lett.* **2020**, *116*, 23.
[3] A. M. Larson, *Nat. Photonics* **2010**, *5*, 1.
[4] R. MacDonald, N. Lawandy, *Opt. Commun.* **1993**, *103*, 345.
[5] Y. Kivshar, *Natl. Sci. Rev.* **2018**, *5*, 144.
[6] B. Sain, C. Meier, T. Zentgraf, *Adv. Photonics* **2019**, *1*, 1.
[7] A. I. Kuznetsov, A. E. Miroshnichenko, M. L. Brongersma, Y. S. Kivshar, B. Luk'yanchuk, *Science* **2016**, *354*, 6314.
[8] V. F. Gili, L. Carletti, A. Locatelli, D. Rocco, M. Finazzi, L. Ghirardini, I. Favero, C. Gomez, A. Lemaître, M. Celebrano, C. De Angelis, G. Leo, *Opt. Express* **2016**, *24*, 15965.
[9] D. Smirnova, Y. S. Kivshar, *Optica* **2016**, *3*, 1241.
[10] F. J. F. Löchner, A. N. Fedotova, S. Liu, G. A. Keeler, G. M. Peake, S. Saravi, M. R. Shcherbakov, S. Burger, A. A. Fedyanin, I. Brener, T. Pertsch, F. Setzpfandt, I. Staude, *ACS Photonics* **2018**, *5*, 1786.
[11] L. Carletti, K. Koshelev, C. De Angelis, Y. Kivshar, *Phys. Rev. Lett.* **2018**, *121*, 033903.
[12] K. Koshelev, A. Bogdanov, Y. Kivshar, *Sci. Bull.* **2019**, *64*, 836.
[13] M. Celebrano, D. Rocco, M. Gandolfi, A. Zilli, F. Rusconi, A. Tognazzi, A. Mazzanti, L. Ghirardini, E. A. A. Pogna, L. Carletti, C. Baratto, G. Marino, C. Gigli, P. Biagioni, L. Duó, G. Cerullo, G. Leo, G. Della Valle, M. Finazzi, C. De Angelis, *Opt. Lett.* **2021**, *46*, 2453.
[14] T. Liu, X. Fang, S. Xiao, *Phys. Rev. B* **2021**, *104*, 195428.
[15] A. Tognazzi, P. Franceschini, D. Rocco, L. Carletti, A. Locatelli, M. Gandolfi, D. Zappa, A. C. Cino, E. Comini, G. Leo, C. De Angelis, *IEEE Photonics Technol. Lett.* **2023**, *35*, 505.
[16] R. C. Miller, *Phys. Rev.* **1964**, *134*, A1313.
[17] C. Ma, J. Yan, Y. Wei, P. Liu, G. Yang, *J. Mater. Chem. C* **2017**, *5*, 4810.
[18] J. Zhou, W. Zhang, M. Liu, P. T. Lin, *Photonics Res.* **2019**, *7*, 1193.
[19] E. Kim, A. Steinbrück, M. T. Buscaglia, V. Buscaglia, T. Pertsch, R. Grange, *ACS Nano* **2013**, *7*, 5343.
[20] P. Tang, D. J. Towner, T. Hamano, A. L. Meier, B. W. Wessels, *Opt. Express* **2004**, *12*, 5962.
[21] P. Castera, A. M. Gutierrez, D. Tulli, S. Cueff, R. Orobtchouk, P. Rojo Romeo, G. Saint-Girons, P. Sanchis, *IEEE Photonics Technol. Lett.* **2016**, *28*, 990.
[22] F. Eltes, G. E. Villarreal-Garcia, D. Caimi, H. Siegwart, A. A. Gentile, A. Hart, P. Stark, G. D. Marshall, M. G. Thompson, J. Barreto, J. Fompeyrine, S. Abel, *Nat. Mater.* **2020**, *19*, 1164.
[23] J. Winiger, K. Keller, D. Moor, M. Baumann, D. Kim, D. Chelladurai, M. Kohli, T. Blatter, E. Dénervaud, Y. Fedoryshyn, U. Koch, S. Pané, R. Grange, J. Leuthold, *Adv. Mater. Interfaces* **2023**, *11*, 1.
[24] H. C. Weigand, Ü.-L. Talts, A.-L. Vieli, V. V. Vogler-Neuling, A. Nardi, R. Grange, *Nano Lett.* **2024**, *24*, 5536.
[25] A. Messner, F. Eltes, P. Ma, S. Abel, B. Baeuerle, A. Josten, W. Heni, D. Caimi, J. Fompeyrine, J. Leuthold, *J. Lightwave Technol.* **2019**, *37*, 281.
[26] Y. Cao, S. L. Tan, E. J. H. Cheung, S. Y. Siew, C. Li, Y. Liu, C. S. Tang, M. Lal, G. Chen, K. Dogheche, P. Yang, S. Pennycook, A. T. S. Wee, S. Chua, E. Dogheche, T. Venkatesan, A. Danner, *Adv. Mater.* **2021**, *33*, 37.
[27] Z. Dong, A. Raju, A. B. Posadas, M. Reynaud, A. A. Demkov, D. M. Wasserman, *ACS Photonics* **2023**, *10*, 4367.
[28] Z. Zheng, L. Xu, L. Huang, D. Smirnova, P. Hong, C. Ying, M. Rahmani, *Phys. Rev. B* **2022**, *106*, 125411.
[29] L. Qu, L. Bai, C. Jin, Q. Liu, W. Wu, B. Gao, J. Li, W. Cai, M. Ren, J. Xu, *Nano Lett.* **2022**, *22*, 9652.
[30] A. Fedotova, L. Carletti, A. Zilli, F. Setzpfandt, I. Staude, A. Toma, M. Finazzi, C. De Angelis, T. Pertsch, D. N. Neshev, M. Celebrano, *ACS Photonics* **2022**, *9*, 3745.
[31] H. Weigand, V. V. Vogler-Neuling, M. R. Escalé, D. Pohl, F. U. Richter, A. Karvounis, F. Timpu, R. Grange, *ACS Photonics* **2021**, *8*, 3004.
[32] P. Girouard, P. Chen, Y. K. Jeong, Z. Liu, S.-T. Ho, B. W. Wessels, *IEEE J. Quantum Electron.* **2017**, *53*, 1.
[33] J.-s. Wang, K.-j. Jin, J.-x. Gu, Q. Wan, H.-b. Yao, G.-z. Yang, *Sci. Rep.* **2017**, *7*, 1.
[34] P. Grahn, A. Shevchenko, M. Kaivola, *New J. Phys.* **2012**, *14*, 093033.
[35] B. I. Edmondson, S. Kwon, C. H. Lam, J. E. Ortmann, A. A. Demkov, M. J. Kim, J. G. Ekerdt, *J. Am. Ceram. Soc.* **2019**, *103*, 1209.
[36] Ü-L. Talts, H. C. Weigand, G. Saerens, P. Benedek, J. Winiger, V. Wood, J. Leuthold, V. Vogler-Neuling, R. Grange, *Small* **2023**, *19*, 50.
[37] A. Karvounis, V. V. Vogler-Neuling, F. U. Richter, E. Dénervaud, M. Timofeeva, R. Grange, *Adv. Opt. Mater.* **2020**, *8*, 17.
[38] F. Kaufmann, G. Finco, A. Maeder, R. Grange, *Nanophotonics* **2023**, *12*, 1601.
[39] R. J. Ong, J. T. Dawley, P. G. Clem, *J. Mater. Res.* **2003**, *18*, 2310.